Received: 7 March 2020 | Revised: 12 June 2020 | Accepted: 26 June 2020

DOI: 10.1002/pip.3317

RESEARCH ARTICLE

PROGRESS IN PHOTOVOLTAICS WILEY

Effect of Na-PDT and KF-PDT on the photovoltaic performance of wide bandgap Cu (In,Ga)Se2 solar cells

Setareh Zahedi-Azad | Matthias Maiberg | Roland Scheer

Institute of Physics, Martin Luther University Halle-Wittenberg, Halle (Saale), Germany

Correspondence
Roland Scheer, Institute of Physics, Martin Luther University Halle-Wittenberg, Halle (Saale) 06120, Germany.
Email: roland.scheer@physik.uni-halle.de

Funding information
Federal Ministry of Economic Affairs and Energy, Grant/Award Number: EFFCIS 0324076C

Abstract

Cu (In,Ga)Se_2 solar cells exhibit higher efficiencies if an appropriate Ga gradient is introduced and if the absorber is doped with sodium (Na) plus a heavier alkali atom such as potassium. However, a Gallium gradient in the presence of Na is challenging because sodium impedes the interdiffusion of elements and influences the gradient. In this contribution, we show that the presence of sodium during growth with the combination of high Ga concentration creates a pronounced gradient that is detrimental for carrier collection. One solution is to avoid Na abundance during absorber growth but to add it to the grown absorber layer via a postdeposition treatment. We investigate the effect of different Na incorporation methods simultaneously with KF-PDT on wide band gap CIGSe absorbers. By preparation on alkali-free substrates and application of alkalis (NaF and KF) onto a grown CIGSe layer, we show by smoothening of the Gallium gradient a large improvement in the solar cell performance from 4% to 8%. Another way to optimize the gradient in the presence of Na is the modification of the three-stage method. This yields the best efficiency of 10% in our laboratory at an integral GGI of ∼0.8. By means of temperature-dependent JV measurements, we show that the additional postdeposition of KF induces a barrier for the diode current. We conclude that KF-PDT induces a new thin layer at the CIGSe surface that has a lower valence band edge relative to the CIGSe bulk and is responsible for the double-diode behavior. This barrier can also explain the V_{oc}(T) saturation at low temperature.

KEYWORDS
compositional gradient, Cu(In,Ga)Se_2, postdeposition treatment, wide bandgap

1 | INTRODUCTION

Increasing the efficiency of CIGSe solar cells still is an ongoing topic. Although the efficiency of small bandgap CIGSe solar cells has surpassed 20%,[1,2] the efficiency of wide bandgap CIGSe solar cells is far below the theoretical Shockley-Queisser limit.[3,4] One of the reasons why small bandgap CIGSe solar cells outperform those with wide gaps is the appropriate bandgap grading of the former.[3,5–8] A bandgap gradient can be realized by compositional gradients of Gallium/Indium or Sulfur/Selenium ratios. The systematic adjustment of the gradient in a multistage evaporation process, however, is challenging because this adjustment is influenced by many parameters such as evaporation rate, substrate temperature,[6] and sodium concentration.[9] If sodium is present during growth, the interdiffusion of the chemical elements is impeded and thus a stronger gradient will be created.[10,11] On the other hand, sodium is mandatory to achieve a high solar cell efficiency with CIGSe.[8] Thus, one

method to incorporate sodium is Na postdeposition treatment of Na-free grown CIGSe absorber. This method allows controlling the sodium amount and at the same time does not prevent interdiffusion of the elements.[12] In effect, steep detrimental Gallium gradients can be avoided.

Postdeposition of heavier alkalis further improves the solar cell efficiency by widening the bandgap at the surface, resulting in higher open-circuit voltages (V_{OC}),[13] provided that the CIGSe layers have the appropriate composition.[14] Recently, it has been shown that doping with potassium can partially quench interface recombination being the V_{OC} limitation for wide bandgap CIGSe solar cells.[13] In this article, we study the interaction between Gallium (Ga) grading and alkali doping in coevaporated wide bandgap CIGSe, aiming at an improved solar cell performance. Coevaporation of CIGSe on Na-containing glass using the three-stage method at temperatures below 625°C gives rise to a pronounced V-shaped gradient. In wide bandgap CIGSe solar cells, this results in current losses at long wavelengths. We show an improved interdiffusion of Indium and Gallium in the absence of sodium during CIGSe growth. In this case, the doping of NaF and KF is conducted after the CIGSe growth. For deeper understanding, a matrix of wide bandgap CIGSe films with different NaF thickness followed by KF is prepared, and the electronic parameters are investigated. Despite great improvements, all electronic parameters cannot be improved simultaneously. Another approach to prepare alkali-doped CIGSe with smoothened compositional grading is the modification of the deposition recipe. Thereby, we achieve the highest efficiencies on Na-containing substrates in this study. At the end, by means of temperature-dependent JV measurement, we show that KF-PDT leads to a barrier for the diode current (and partly for the photo current). A barrier for the diode current was recently proposed for small band gap CIGSe treated with RbF.[15] The current–voltage curves simulation by Synopsys TCAD assume that the alkali PDT induces a new phase, probably K(In,Ga)Se_2, at the CIGSe surface that has a lowered valence band edge relative to the CIGSe layer.

2 | EXPERIMENTAL SECTION

2.1 | Solar cell processing

CIGSe films were deposited by coevaporation in a three-stage process (Figure 1).[16] In the first stage of the process, the substrate temperature was 400°C. In the second and third stages, it nominally was 625°C. During the CIGSe deposition, the ratio of Selenium to metal fluxes approximately was Se/Me ~ 7/1. Five conceptual different types of sample were prepared, which are described in Table 1. These five samples are grown with three different recipes given in Figure 1. Sample A1 was grown by recipe (a) on a Mo-sputtered soda lime glass (SLG), where sodium could diffuse from the glass through the absorber (nonbarrier substrate). In the same run, an additional CIGSe sample with the notation A2 was grown on a Mo-coated SLG with an alkali diffusion barrier (SiO_xN_y) to prevent diffusion of Na and K from the SLG (barrier substrate). Note that recipe (a) is the normal three-stage recipe with no Indium and Gallium deposition in the second stage. After CIGSe deposition, the samples were cooled down to 450°C while keeping the Selenium evaporation rate at one third of its former value and with constant Se flux KF was evaporated with an evaporation rate of 0.1 Å/s for 800 s (Figure 1A).

In another series of experiments, Cu(In,Ga)Se_2 absorbers were grown on barrier substrates, and the deposition recipe (b) in Figure 1B was used. After deposition of the CIGSe layer, the samples were cooled down to 450°C and treated first with NaF and then with KF under constant Se flux. The alkalis were evaporated with an evaporation rate of 0.1 Å/s. The evaporation chamber is equipped with separate effusion cells for NaF and KF; therefore, the postdeposition of NaF and KF was conducted without breaking the vacuum (Figure 1B). In order to find the best electrical parameters, we prepared a matrix of samples where the thickness of NaF and KF was varied in the intervals 8–35 and 8–25 nm, respectively. In the next section, it will be shown that for samples grown with recipe (b), Sample B1 with 15-nm NaF and 20-nm KF-PDT has a superior efficiency.

In the last set of experiments, Sample C1 was prepared on a nonbarrier substrate using the modified growth recipe (c) where the absorber goes through the Cu-rich and Cu-poor phases, but Ga is evaporated throughout the second stage (Figure 1C). The evaporation of Ga in the second stage allows tuning of the Ga-profile. Due to the presence of Ga in the second stage, the first stage had to be shorter in order to obtain the same thickness as of the other samples. Furthermore, a higher In evaporation rate was set in order to have the same GGI concentration like in the other samples. After deposition of the CIGSe layer, Sample C1 was doped with KF like in process (a). A sample with the notation sample C2 was also prepared according to recipe (c) on nonbarrier substrate but without KF-PDT, which will be

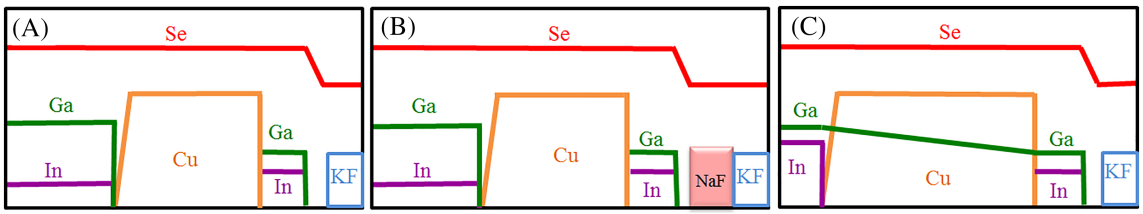

FIGURE 1 Wide bandgap CIGSe deposition recipes. (A) shows recipe (a) without NaF-PDT but with KF-PDT for samples A1-A2. (B) shows recipe (b) with NaF-PDT and KF-PDT for the barrier substrate. Recipe (c) is shown in (C) with shortened first stage, extended second stage and evaporation of Ga, and KF-PDT for the nonbarrier substrate (Sample C1) [Colour figure can be viewed at wileyonlinelibrary.com]

TABLE 1 Overview of investigated samples

ID	Recipe	Substrate	Alkali-PDT	Section	Figures	Simulation in section
A1	(a)	Nonbarrier	8-nm KF	3.1, 3.2, 3.3	2, 3, 5	-
A2	(a)	Barrier	8 nm KF	3.1, 3.2, 3.3	2, 3	-
B1	(b)	Barrier	15-nm NaF + 20 nm KF	3.3, 3.4	5, 6, 7	4
C1	(c)	Nonbarrier	8-nm KF	3.2, 3.3, 3.4	3, 5, 6, 7	4
C2	(c)	Nonbarrier	w/o PDT	3.3, 3.4	6, 7	4.1

Note. The type of recipes refers to Figure 1. Rubrics "Section" and "Figures" indicate the sections and figures of sample appearance.

discussed in Section 3.4. An overview of the investigated samples is given in Table 1.

Chemical bath deposition (CBD) of a 50-nm thick CdS layer and sputtering of i-ZnO/ZnO:Al (100 nm/300 nm) were performed to obtain the finished solar cell. Finally, a Ni/Al/Ni grid as a front contact was evaporated. The area of the cells was defined by mechanical scribing.

2.2 | Characterization

The composition of CIGSe films was measured by energy dispersive X-ray (EDX) spectroscopy using an acceleration voltage of 30kV. A set of different samples with different KF and NaF thicknesses with the GGI ([Ga]/([Ga] + [In])) in the range of 0.8 ± 0.03 and [Cu]/([Ga] + [In]) (CGI) in the range of 0.85–0.92 were examined. The cross section of the absorbers was studied with a scanning electron microscope (SEM; ZEISS) with an acceleration voltage of 5 kV. The compositional depth profiles were measured by means of glow discharge optical emission spectroscopy (GDOES) in a Spectruma GDA750, with 2.5-mm anode diameter.

The current density‐voltage (JV) curves of the finished solar cells were determined under simulated standard test conditions (AM1.5G, 298 K, 1000 Wm^{-2}) using a four-terminal-sensing measurement setup. The external quantum efficiency (EQE) was measured using lock-in technique. The devices were illuminated by monochromatic light from a 300-W Xenon lamp passing through a monochromator (Oriel Cornerstone). For calibration, a Silicon reference solar cell was used. The optical bandgap (E_g) was extracted by linear extrapolation of the leading edge of the EQE.

Temperature-dependent current–voltage (JVT) measurements were conducted in a cryostat with closed-helium cycle within a temperature range 100 to 300 K in 10 K steps. Illumination was provided by a Xenon lamp from Science-tech with a calibrated AM1.5G spectrum. Due to the heat of the lamp, the minimum temperature that could be achieved was 100 K upon white light illumination.

2.3 | Device simulation

The simulations were performed by Synopsys® TCAD using a one-dimensional model represented by a mathematical mesh, which is generated by Delaunay triangulation.[17,18] It is emphasized that Sentaurus TCAD uses the Fermi‐Dirac statistics that allows for accurate results even at low temperatures.

3 | RESULTS AND DISCUSSION

3.1 | Microstructural effects

First, the influence of Na on the microstructure of wide-bandgap CIGSe is investigated. Morphological changes by the influence of sodium have been investigated by many researchers and an increase[19] or decrease[20] of the grain size in the absence of sodium has been reported. SEM cross-sectional images of Samples A1 and A2 are shown in Figure 2A,B, respectively. In our lab, wide-bandgap CIGSe absorbers (GGI: 0.8) grown on nonbarrier substrates are characterized by small grains (Figure 2A). For CIGSe films grown on barrier substrates (absence of sodium during growth), larger grains have been formed as visible in Figure 2B. This motivated the application of barrier substrates for the systematic variation of Na and K in Figure 4.

3.2 | Depth profile analysis

The GDOES depth profiles of the GGI of Samples A1 and A2 are shown in Figure 3. The CIGSe layers were grown in the same run (recipe (a)) on the two different substrates (barrier and nonbarrier substrates). All the CIGSe absorbers show a reduction of Gallium in the first ∼200 nm, although as shown in Figure 1, no reduction of Gallium was designed in the last stage of the deposition process. Sample A1 exhibits a very strong GGI gradient towards the back contact as well as towards the front contact, thus a very deep notch (Figure 3). In contrast, the notch of Sample A2 is less deep. This indicates that Na impedes the interdiffusion of Ga and In during growth and therefore induces the formation of a steeper [Ga]/([Ga] + [In]) gradient.[9] Sample C1 is also presented in Figure 3. It can be seen that evaporation of Ga in the second stage smoothens the gradient profile (recipe (c) versus recipe (a)) and reduces the front grading. In the next section, we show that Sample C1 has the best solar cell performance. It must be noted that the integral GGI values of all samples is ∼0.80 ± 0.03, which corresponds to a bandgap value of ∼1.45 eV.

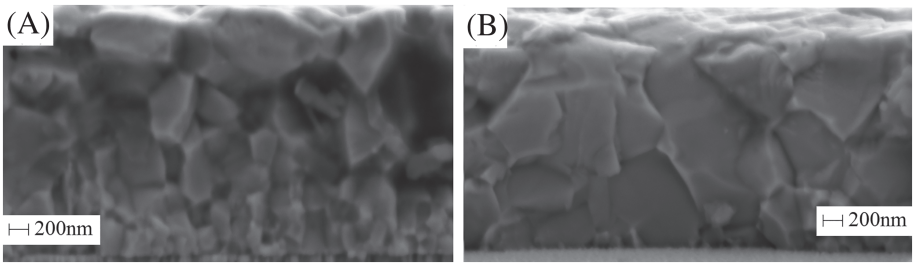

FIGURE 2 Cross-sectional scanning electron microscope (*SEM*) images of CIGSe absorbers with GGI = 0.8 grown on the Mo coated (A) nonbarrier substrate (Sample A1), (B) barrier substrate according to recipe (a) in Figure 1 (Sample A2). Larger grains are observed for the sample grown in the absence of Na

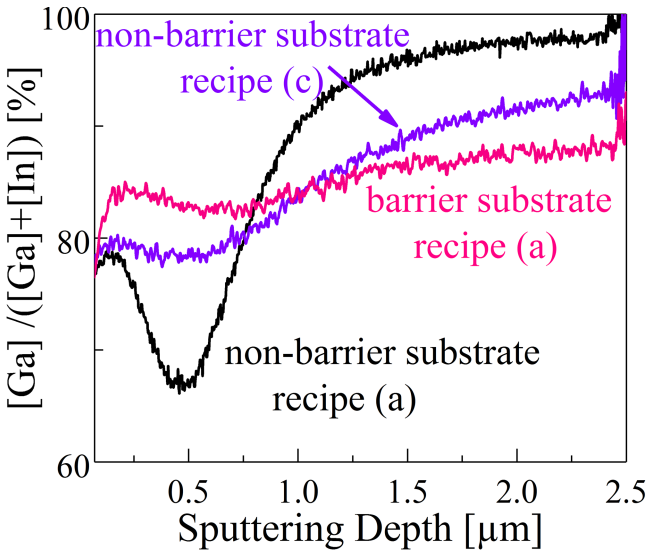

FIGURE 3 GGI profiles of different substrates with an integral GGI value ~ 0.80 ± 0.03 (with 8-nm KF) [Colour figure can be viewed at wileyonlinelibrary.com]

3.3 | Solar cell parameters

The effect of NaF and KF thicknesses was investigated in a wide range of 8–35 and 8–25 nm, respectively, in order to map out possible multiple efficiency maxima. The solar cell parameters of CIGSe solar cells on barrier substrates as a function of NaF and KF thicknesses are presented as a color map in Figure 4. The best efficiency for wide-bandgap CIGSe solar cells was achieved for 15-nm NaF and 20-nm KF postdeposition treatment (Figure 4D). The combination of these thicknesses is very close to the one of high efficiency small bandgap CIGSe solar cells reported in the literature (~26-nm NaF and ~15-nm KF).[2] Comparable data for wide-bandgap CIGSe otherwise do not exist.

In Figure 4A, the V_{OC}-deficit, $\Delta V_{OC} = E_g/q - V_{OC}$, for different samples is plotted. The difference between the maximum possible current density and the measured current, $\Delta J_{SC} = J^{max}_{SC} - J^{*}_{SC}$, is shown in Figure 4B. The current density J^{*}_{SC} is derived from integration of the measured EQE over AM1.5G. The maximum possible current density J^{max}_{SC} is the integrated AM1.5G photon flux spectrum times the elementary charge. It has to be noted that the grid is not included in the EQE measurement; as a result, the J^{max}_{SC} is the active area value.

In Figure 4, it can be observed that the smallest ΔV_{OC} is not combined with the lowest ΔJ_{SC}; and for samples with the lowest ΔJ_{sc}, the ΔV_{OC} is rather high (and FF low). In addition, we see that too large KF-PDT thickness reduces the FF despite a small ΔV_{oc}. The reason may be a reduced collection efficiency at forward bias (see Section 4.4 and Figure S1).

In Figure 5A, the JV curves of Samples A1, B1, and C1 are depicted. Samples A1 and C1 have the same KF thickness of 8 nm, and Sample B1 has 15-nm NaF and 20-nm KF postdeposition treatment (see Table 2). The V_{OC} value of sample B1 in Figure 5 is slightly lower than the V_{OC} in Figure 4 because for the solar cells in Figure 5, we have used another TCO with lower resistivity. Note that, according to our former experiments, for nonbarrier samples where Sodium is supplied by the substrate, 8-nm KF provides the highest solar cell performance on wide-bandgap CIGSe.[21]

Sample A1 has a very low FF and low J_{SC}. The FF clearly improves, and J_{SC} slightly increases when CIGSe as of Sample B1 was prepared by recipe (b). This indicates that the strong front grading as shown in Figure 3 traps the electrons in the notch, where they can recombine with holes reducing the J_{SC}.[6] This is in line with Gloeckler's simulation, in that a strong front grading reduces J_{SC} and FF.[8] Therefore, a modification in the compositional grading is required to improve the electronic parameters. The electrical parameters of the investigated solar cells are summarized in Table 2.

The best efficiency is achieved for Sample C1. This we assign to the removed front gradient (Figure 3A). In Figure 5B, the spectral responses of the selected samples in Table 2 are presented. Although Sample A1 shows a very weak carrier collection in the long wavelength range (600–900 nm), this is substantially improved for Sample B1. The thereby improved current density results in higher cell efficiency (see Table 2). This indicates that indeed the compositional gradient is an important issue in wide-bandgap CIGSe solar cells, and considerable attention must be paid to deposition details of the wide-gap CIGSe absorbers. The underlying reason besides the small diffusivity of Gallium atoms in CIGSe absorber is the presence of Sodium that hinders the interdiffusion of metals.[22]

It can be observed that the spectral response of Sample B1 is lower compared with Sample C1 at long wavelengths. The reason might be the absence of the gallium gradient in combination with a small electron diffusion length. In order to find the responsible current limitation mechanism, we measured the JVT in darkness and under illumination. By doing so, Sample A1 is no longer our subject of study, and Samples B1 and C1 will be compared.

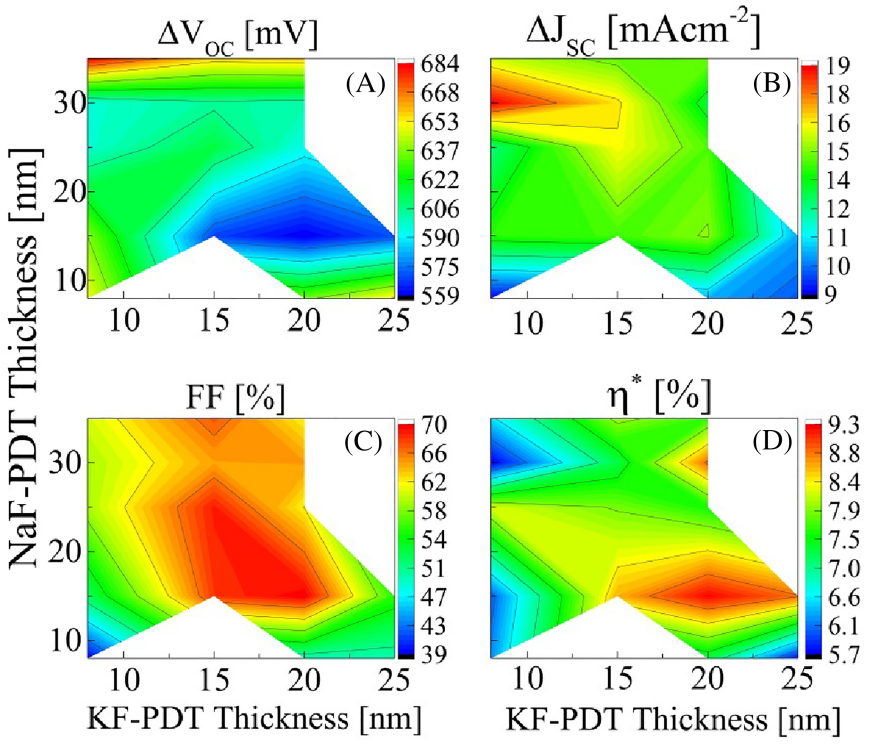

FIGURE 4 Influence of NaF-PDT (8, 15, 25, and 35 nm) and KF-PDT (8, 15, 20, and 25 nm) thicknesses on the solar cell parameters. All absorbers prepared on barrier substrate according to recipe (b) in Figure 1. The integral GGI of used absorbers is 0.80 ± 0.05. (A) ΔV_{OC} is the difference between the measured E_g/q and the measured V_{OC}, (B) ΔJ_{SC} is the difference between the maximum theoretical current density and the measured current density, (C) FF, and (D) $\eta^*$is the efficiency of active area [Colour figure can be viewed at wileyonlinelibrary.com]

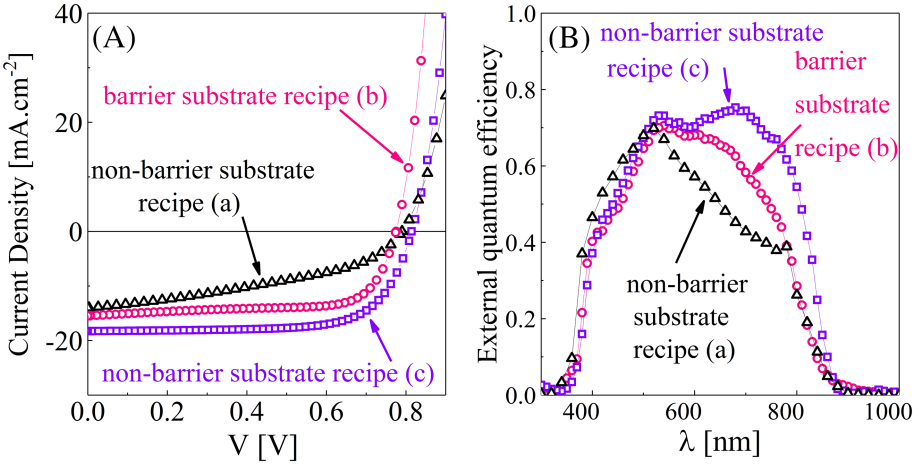

FIGURE 5 (A) JV and (B) external quantum efficiency of three different samples grown by recipes (a)-(c) from Figure 1. The highest EQE signal can be achieved when CIGSe is prepared with a modified multistage process (recipe (c)) on a nonbarrier substrate [Colour figure can be viewed at wileyonlinelibrary.com]

3.4 | Temperature-dependent JV characterization

Temperature-dependent JV curves of Samples B1 and C1 are shown in Figure 6B,C, respectively. In order to investigate the influence of KF on JVT, Sample C2 is also shown here. All samples have the same bandgap value, and the lower open-circuit voltage of Sample C2 (see Table 2) is due to absence of potassium.[13]

All the samples in Figure 6 show a crossover between the dark and light JV curves, that is, at forward bias the current under illumination is higher than in darkness. This anomaly hints to a barrier for the diode current in the dark and has been reported frequently for small bandgap CIGSe solar cells.[23–25] In addition, Figure 6B,C reveals a double-diode behavior in the light JV curves for the KF-treated samples (B1 and C1), and Sample C2 (without KF-PDT) does not show a blocking behavior at low temperatures (Figure 6A). Furthermore, the JV distortion of Sample B1 in Figure 6B is slightly stronger than that of Sample C1, presumably due to a thicker KF layer on Sample B1. As mentioned previously, Sample B1 has 20-nm KF and Sample C1 has

TABLE 2 Electronic parameters of the five samples from Figures 3 and 5

ID	GGI	V_{OC} (mV)	J^*_{SC} (mAcm^{-2})	FF (%)	η^* (%)
A1	0.80	790.2	14	41.1	4.54
A2	0.80	-	-	-	-
B1	0.77	775.3	15.48	70.4	8.44
C1	0.78	814.2	18.3	70.8	10.54
C2	0.78	748	16.5	61.6	7.6

Note. J^*_{SC} is calculated by integrating the EQE response with the AM1.5G spectrum. η^* is the efficiency of active area and is calculated using J^*_{SC}.

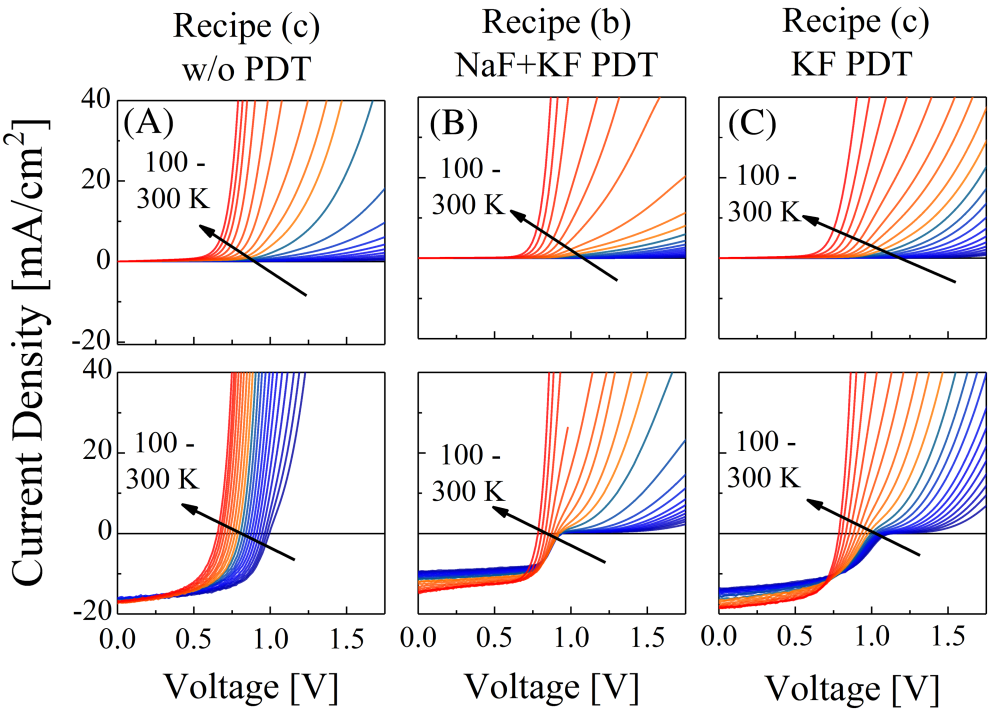

FIGURE 6 Temperature-dependent JV curves (100 to 300 K in 10 K steps) of Samples (A) C2, (B) B1, and (C) C1. All CIGSe layers have a GGI of 0.83. Measurement in darkness (top) and under white light (bottom) [Colour figure can be viewed at wileyonlinelibrary.com]

8-nm KF-PDT. Weiss et al. have observed for small bandgap CIGSe cells that as the thickness of RbF-PDT increases, a larger barrier is induced.[15]

For small bandgap CIGSe cells with NaF and KF-PDT, a rollover of the JV curve at low temperatures was observed, which was explained by a barrier at the Mo/CIGSe interface.[26] Kodalle et al. have also reported a barrier for the photocurrent for RbF-treated CIGSe cells.[27] But our alkali-treated samples exhibit a different behavior; the light JV curves show a double diode behavior, that is, a clear resumption of the injection current upon higher voltage, and not any saturation of the current density, which is a behavior that has not been reported for KF-treated CIGSe cells. In the case of a barrier at the back contact, both the dark and the illuminated JV curves have to show current saturation at large forward bias,[28] which is not observed here. Therefore, we conclude that the double-diode behavior in Figure 6 is due to a barrier at the front and not at the back contact.

Another important finding from Figure 6 is that the short-circuit current density (J_{SC}) of the alkali-treated samples (B1 and C1) is temperature dependent (Figure 6B, C). The photo current of the alkali-treated samples (B1 and C1) reduces as the temperature decreases (Figure 6B, C), and the short-circuit current density of the untreated sample (C2) is not influenced by temperature (Figure 6A). Also, the variation of V_{OC} with temperature is of interest. Therefore, the V_{OC} data from Figure 6 are plotted in Figure 7A as a function of temperature. The extrapolation of $V_{OC}(T)$ measured at high temperatures ($T > 200$ K) towards $T = 0$ K roughly gives the activation energy of the saturation current density, E_a.

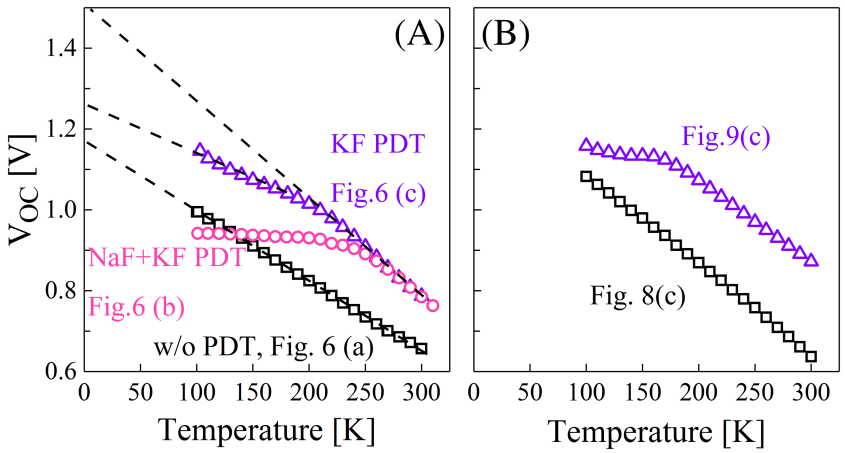

FIGURE 7 (A) Experimental open-circuit voltage (V_{OC}) versus temperature of samples from Figure 6A–C. Dashed lines depict extrapolation to 0 K. (B) Simulated $V_{OC}(T)$ data for the models in Figures 8 and 10A extracted from plots Figures 8C and 10C [Colour figure can be viewed at wileyonlinelibrary.com]

$$V_{oc}(T) = \frac{E_a}{q} - \frac{A(T)kT}{q} \ln\left(\frac{J_{00}}{J_{sc}\eta(V_{oc})}\right). \quad (1)$$

Here, A(T) is the (possibly temperature dependent) diode quality factor, J_{00} the reference current density, J_{SC} the short circuit current density, and $\eta(V_{OC})$ the collection efficiency at open circuit. The measurement result in Figure 7A indicates that E_a of the untreated cell (Sample C2) is smaller than the bandgap of E_g = 1.5 eV ($E_a \approx 1.2$ eV). The two alkali-treated samples, to the contrary, exhibit E_a approximately equaling the bandgap (E_a = 1.5 eV). This indicates that the non-treated device is limited by interface recombination (IFR)[29] and that the KF treatment modifies the surface of the absorber. A possible modification is a bandgap widening that could keep the cell within the regime of IFR but with higher activation energy or which could bring the cell into bulk recombination. In a previous study,[13] it is shown that both mechanisms are possible. For the particular device in Figure 7A, the time-dependent $V_{OC}(t)$ transients exhibit a negative slope.[4] A negative slope of $V_{OC}(t)$ points to a dominant recombination path at the interface because the recombination is controlled by holes at the interface ($R = p\,S_p$). With the increase of the doping density under illumination, the hole barrier decreases. The reduced hole barrier increases the hole density at the interface and thus the recombination rate at the interface. The increased recombination rate at the interface results in a V_{oc} drop under illumination.[4] Thus, regardless of the extrapolated $V_{OC}(T)$ value, all cells in Figure 7A are limited by interface recombination (see Figure S2). We emphasize that for individual cells with GGI = 0.8, interface recombination may be quenched.[13]

In summary, we observe four distinct features in the JV curves of our cells: (1) a crossover between light and dark JV curves for untreated and KF-PDT-treated cells. Exclusively for KF-treated solar cells, we find in addition (2) a JV distortion (double-diode behavior), (3) a temperature-dependent short-circuit current density ($J_{SC}(T)$), and (4) a saturation of $V_{OC}(T)$ towards low temperature. In the following, we try to find a model that could explain these effects. We start to model the crossover for the untreated sample (C2) and then try to extend the model for KF-treated samples (B1 and C1).

4 | MODEL CONSIDERATIONS

4.1 | Modeling the crossover

In order to bring out a crossover, an electron barrier for the injection (forward) current is required whose barrier height reduces upon illumination.[28] Such an illumination-dependent electron barrier can be modeled by an illumination-dependent potential drop in the buffer layer.[28] A high density of deep acceptors in CdS with very different capture cross sections for carriers ($\sigma_p >> \sigma_n$)[24] can serve this purpose. In darkness, the acceptor states are occupied by electrons compensating the ionized donors. This high compensation and low net doping causes a large potential drop in the CdS layer. Upon illumination, the acceptor states in the CdS are filled by holes, become neutral, the compensation is reduced, and a higher net positive charge (by uncompensated donors) leads to a band bending in CdS. This reduces the electron barrier.[30] For simulation, a net doping of the buffer layer of 1×10^{15} cm^{-3} provided by 5×10^{18}-cm^{-3} donors and 4.999×10^{18}-cm^{-3} compensating acceptors was used. The ratio of capture cross sections was programmed to $\sigma_p/\sigma_n = 10^5$. This high asymmetry is necessary in order to bring out the crossover at low temperatures in close agreement with Gloeckler et al.[25] Due to the wide bandgap of the CIGSe absorber, a negative conduction band offset between CIGSe and CdS was programmed (ΔE_C = –0.20 eV). For all layers in the simulation, midgap defects similar to a previous study[28] were implemented (see Table S1).

The resulting band diagram and the simulated dark and illuminated JV curves are shown in Figure 8A‐C. It can be observed that the JVT curves upon white light illumination do not show any distortion but in darkness, the current density becomes reduced, particularly at low temperatures. Thus, the photo-doping of the CdS, which reduces the barrier for the electron current in the conduction band (see Figure 8B), can explain the crossover between the dark and light JV curves. This applies both to the alkali-treated (B1 and C1) and untreated (C2) samples.

An alternative model to explain the crossover is a high density of acceptor states in the absorber's near interface region.[23] In equilibrium, the negative charge density of the p^+ layer reduces the voltage drop in the absorber and forms a large potential drop in CdS. Upon illumination, holes, photo-generated in the buffer layer and transported to the p^+ layer, reduce the acceptor charge in the p^+ layer and thereby reduce the electron barrier. But the p^+ layer eliminates the inversion and results in a kink (barrier for the photocurrent) at low temperatures.[31] Therefore, in addition to the p^+ layer, a high density of donor states at the interface was introduced in order to preserve the inversion. Thus, in the corresponding model (p^+ layer), two assumptions were required to explain the crossover of wide-gap CIGSe cells (see Figure S3), whereas in the previous model, just deep acceptor states in CdS were demanded. We proceed to use the model with CdS impurities (Figure 8) due to its smaller number of necessary assumptions.

4.2 | Modeling $J_{SC}(T)$

A temperature-dependent J_{SC} was also reported for KF-treated small bandgap CIGSe solar cells.[32] There, it was assumed that KF-PDT induces a shallow donor state below the conduction band of CIGSe (below E_C) that can act both as recombination center and as trap state depending on temperature.[32] At low temperature, the electrons captured in the defect state recombine instead of being re-emitted. This reduces J_{SC}. At higher temperatures, the electrons are re-emitted from the defect state before they recombine and thus can contribute to J_{SC}.[32] An alternative explanation for the temperature-dependent J_{SC} would be a mobility of electrons $\mu_e(T)$, which is strongly varying with temperature. This would mean that the carrier scattering mechanism is drastically changing upon KF treatment providing a higher temperature dependence than without KF. For the simulation in Figure 10C,

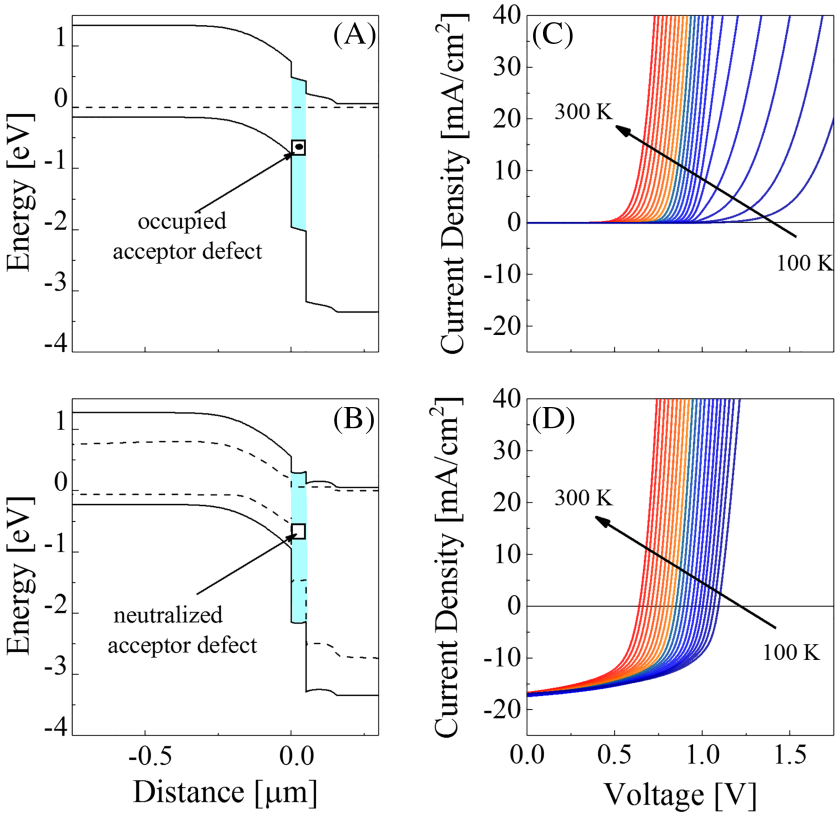

FIGURE 8 Simulation results with acceptor states of high density in CdS for Sample C2 (E_g: 1.5 eV). (A) Band diagram in equilibrium, (B) band diagram at zero voltage under illumination, (C) JV(T) in darkness, and (D) JV(T) under illumination in the range T = 100–300 K in 10 K steps. The acceptor defects in CdS are shown as a rectangle, which are filled with electrons in darkness and are neutralized under illumination [Colour figure can be viewed at wileyonlinelibrary.com]

we have followed Scenario 1 and included defect states with asymmetric capture cross sections below the CIGSe conduction band (for parameters, see Table S2). Similar to the experimental data in Figure 6, the short-circuit current density comes out temperature dependent by simulation in Figure 10C.

4.3 | Modeling the double-diode behavior

In Figure 6B, C, a double-diode behavior was observed for the KF-PDT-treated samples (B1 and C1). This form of illuminated JV curve is a sign for a secondary barrier in the solar cell.[30,33] In contrast to a kink that occurs in the third or fourth quadrant of the JV curve and that is due to a barrier for the photo-current,[28] the resumption of the injection current at high forward bias, leading to the double-diode behavior, occurs in the first quadrant. It indicates a barrier for the diode current that is not removed by illumination. First, we discuss the case without KF treatment (Sample C2) where no double-diode behavior is observed in Figure 6A. The band offset between a wide-gap CIGSe absorber, and the CdS buffer is negative ($\Delta E_C < 0$),[34,35] that is, of cliff type (Figure 8). This cliff has to be overcome by electrons to carry the diode current. For large forward bias (Figure 9A2), an accumulation layer for electrons on the CdS side and an accumulation layer for holes on the CIGSe side is formed (note that this simulation requires use of Fermi-Dirac statistics implemented in Sentaurus TCAD). Both electron and hole densities form a double layer of equal charge density as depicted in Figure 9A2. The high density of electrons on the CdS side now allows thermionic emission of electrons over the remaining barrier. This explains why there is no double-diode behavior for the untreated cell (Sample C2) in experiment (Figure 6) and simulation (Figure 8). However, if the two accumulation layers for *n* and *p* become more distant through implementation of an additional layer, the charge densities in the accumulation regions reduce (see Figure 9B2), and the electron concentration (at intermediate voltage bias) does not suffice to drive a high current by thermionic emission. This brings out the double-diode behavior also in simulation (Figure 10). Only under strongly increased simulated voltage bias, the thermionic emission current is reestablished as is the case for the experimental JV curve of KF-PDT-treated devices in Figure 6 (Samples B1 and C1). In the simulations of Figures 9B and 10, a surface layer formed by the KF-PDT is used, which has the following properties: (i) a conduction band alignment to the underlying CIGSe because a positive spike would result in a kink in the fourth quadrant; (ii) aligned valence band edges at the SL/CdS interface because as suggested, the SL has a large bandgap value;[36,37] and (iii) donor states present at the newly formed CIGSe/SL interface because these specific cells were limited by interface recombination (see Table S2). It has to be reminded that if the cells were not limited by recombination at the hetero-interface, the interface states at the CIGSe/SL could be removed. All other physical properties such as doping density and mobility are programmed identical to the CIGSe layer. The resulting band diagram and the simulated JV(T) curves are shown in Figure 10A-C. Again, the crossover is simulated with deep acceptor states in the buffer layer and the J_{SC}(T) by shallow donor states below the conduction band in the CIGSe absorber. Comparing Figure 10A with Figure 8A reveals that the main difference of the band diagrams

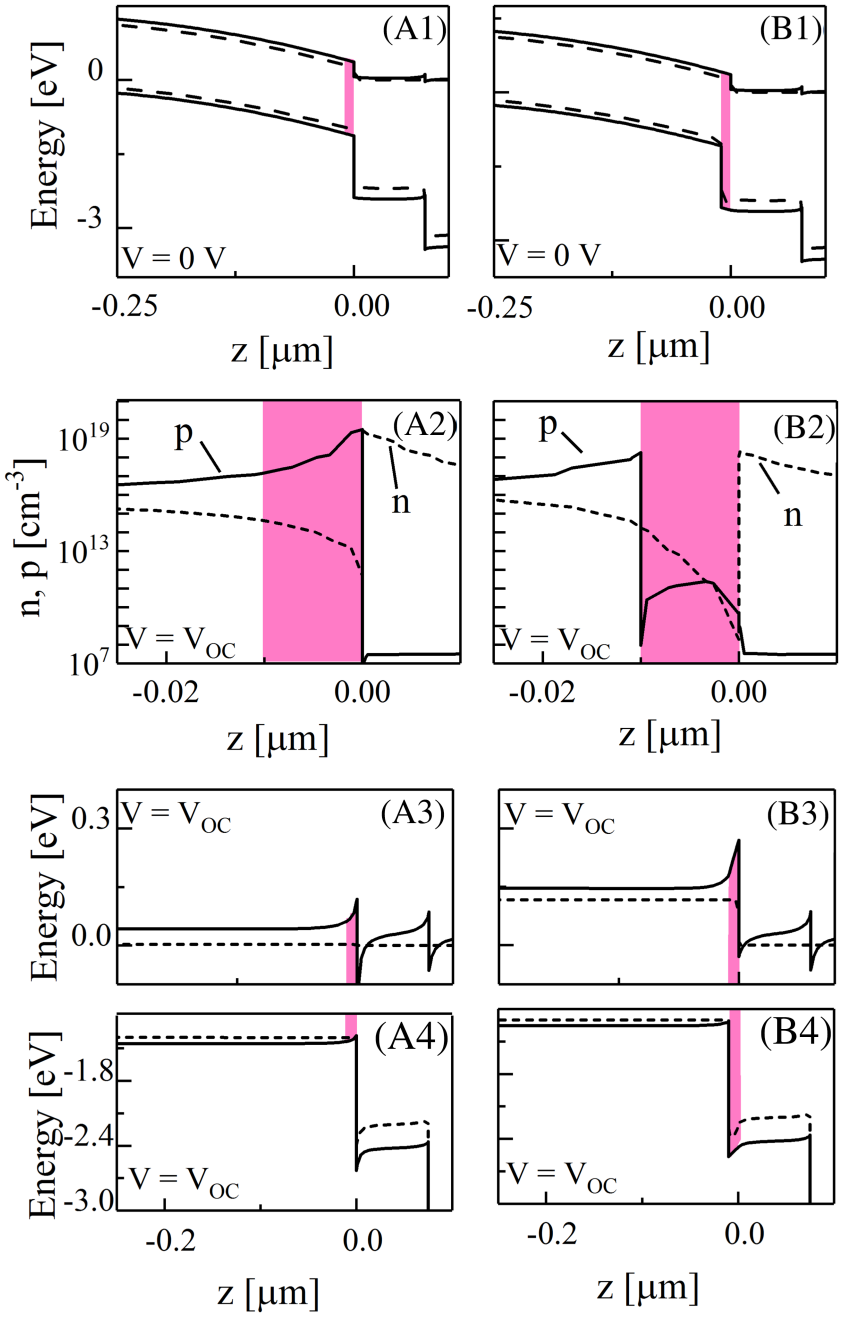

FIGURE 9 Simulated band diagram and carrier densities for a device without (left column) and with (right column) SL at T = 100 K. (A, B) Band diagram at V = 0 under illumination. (A2, B2) Carrier densities in CIGSe/SL/CdS structure. (A3, B3) E_C and E_{Fn} at V = V_{OC} and (A4, B4) E_V and E_{Fp} at V = V_{OC}. The pink layer is the surface layer [Colour figure can be viewed at wileyonlinelibrary.com]

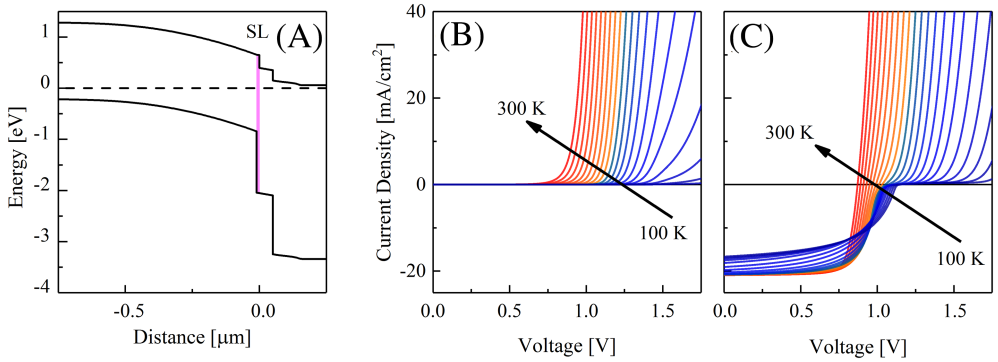

FIGURE 10 Simulation results of CIGSe/SL/CdS/i-ZnO/ZnO:Al heterostructures. (A) Band diagram in equilibrium. (B) Dark and (C) illuminated JV(T) curves in the range T = 100–300 K in 10 K steps [Colour figure can be viewed at wileyonlinelibrary.com]

is the local position of the valence band discontinuity that, by introducing the SL, is energetically shifted downward with respect to the conduction band discontinuity. In Figure 10C, it is visible that this band diagram produces the double-diode behavior as found in the measurement results of the alkali-treated sample in Figure 6. Above V_{OC}, the simulated JV curves at low temperature show a plateau at around zero current in case of the applied SL in Figure 10A. In our simulation, the tunneling between the layers was turned off. By simulation, it was found that reducing the SL thickness to 5 nm (instead of 10 nm in Figures 9B and 10) substantially reduces the double-diode behavior. On the other hand, increasing the thickness of the SL to 15 nm in simulation reduces the simulated fill factor at room temperature. This can explain the reducing FF upon higher KF-PDT thickness as found in Figure 4. These findings indicate that the thickness of the SL is in the range of 10 nm.

4.4 | Modelling the V_{oc} saturation

Figure 7B gives the data of V_{OC}(T) simulated for the devices in Figures 8 and 10. As for the untreated experimental device in Figure 6, an overall reduced V_{OC}(T) is simulated in Figure 7B (black open squares), which extrapolates to ~1.29 V at 0 K. The simulated small extrapolated V_{OC}(0 K) indicates the dominance of interface recombination under open-circuit condition, which was programmed by defect states at the CIGSe/CdS interface (see Table S1). The V_{OC}(T) curve of the untreated device can be fitted by a mostly linear relation over the complete temperature range according to Equation 1.

Figure 7B also includes the simulated V_{OC}(T) for the solar cell in Figure 10 (violet open triangles), which shall represent the KF-treated device. By principle agreement with the experimental curve in Figure 7A, a saturation of V_{OC}(T) towards low temperatures is simulated. This saturation is the result of a reduction of the collection efficiency η(V) at high voltage. Consulting Figure 9B3, an electron barrier in the conduction band, formed by the accumulation layer at distance −0.01 μm plus the potential drop in the SL, can be seen. This barrier impedes the electron current towards the *n* side of the junction at low temperature and leads to a small η (V_{OC}) for the device in Figure 10A. Indeed, the simulated collection efficiency η(V) in Figure S4 shows the reduction of η(V) for high voltages in the presence of a SL. In consequence, the V_{OC}(T) for the device with SL deviates from the linear behavior at low temperatures. This deviation is similar to a back barrier.[38,39] Also, the untreated device shows a barrier for the photocurrent in Figure 9A3. However, this barrier consists only of the band bending in the accumulation layer and therefore is smaller than the barrier from accumulation layer plus potential drop in the SL. Thus, the potential drop in the SL is a result of the lowered valence band edge.

5 | DISCUSSION

Table 3 summarizes the experimentally detected phenomena of the JV(T) analysis and the applied simulation features. Three of four phenomena found in the high Gallium CIGSe samples are connected with the application of the heavy alkali KF treatment.

Both the double-diode behavior and the V_{OC}(T) saturation can be explained by the formation of a surface layer (SL) on the wide-bandgap CIGSe. Recent reports on alkali-treated samples reveal that alkalis can form a SL on top of CIGSe that has a larger band gap.[37,40–44] For example, Handicks et al.'s measurements on small bandgap CIGSe indicate that this SL has both band edges more distant from the Fermi level as compared with CIGSe.[41] Pistor et al.[44] have shown that KF-PDT widens the bandgap of the CIGSe surface by lowering the valence band edge. The experimental measurements of Handick et al. show that a $K(In,Ga)Se_2$ phase has a bandgap value of 2.6 eV.[41] Hauschild et al. measurements indicate that also RbF-PDT modifies the surface by lowering the valence band edge.[37] Cesium, on the other hand, does not seem to form an SL.[45] All these findings are for low bandgap CIGSe; no such measurements are performed for high-bandgap CIGSe. Nevertheless, we similarly assume that a surface layer of $K(In,Ga)Se_2$ has formed at the surface of the KF-treated wide bandgap CIGSe. Thus, here, it is postulated that the SL introduced in the band diagram as depicted in Figure 10 is made of $K(In,Ga)Se_2$. In Section 4.3, some physical properties (i)–(iii) of this layer where anticipated. Of these, the aligned conduction band (i) is important because a positive ΔE_c (spike) between CIGSe and the SL can easily lead to a kink in the illuminated JV curve (fourth quadrant distortion). The aligned valence band (ii) between SL and CdS results from the bandgap of roughly 2.7 eV assumed for the SL. And (iii) defects states at the CIGSe/SL interface are necessary in order to render interface recombination the dominant mechanism limiting V_{OC} for KF-treated wide-bandgap devices. With these properties anticipated, the double-diode behavior and the V_{OC}(T) saturation can be explained. Also, the persistent interface recombination for KF-treated devices can be explained. However, the interface states (iii) have not been detected so far. Voltage-dependent admittance measurements did not show any defect at high forward bias in our measurements (not shown). This means that the distance from any band edge is too deep to be detected. The puzzling observation that some but not all cells could be cured from interface recombination by the KF-treatment[13] points to the critical role of the absolute state density at the CIGSe/SL interface. If this density is lower than at the CIGSe/CdS interface, higher

TABLE 3 Configurations for simulation of the observed anomalies for the KF-treated and untreated samples of Figure 6A–C

Sample	Properties	Crossover	J_{SC}(T)	Double-diode behavior	V_{OC}(T) saturation
C2	w/o PDT	Acceptor state in CdS	-	-	-
B1, C1	KF-PDT	Acceptor state in CdS	Trap state in CIGSe	Low valence band edge of SL	Potential drop in SL

V_{OC} values can be obtained, in agreement with the experimental findings.

An effect that cannot be explained by the SL is the $J_{SC}(T)$ variation in Table 3. This effect requires some Potassium-induced bulk effect in CIGSe. Although studies have shown that alkalis in CIGSe are mostly allocated at grain boundaries,[46] also the formation of a bulk defect has been found by Pianezzi et al., both for KF co-evaporation and (with smaller density) for KF-PDT.[32] Pianezzi et al. using deep-level transient spectroscopy assigned this defect to a minority carrier trap about 0.3 eV below the conduction band.[32] In our simulation of the $J_{SC}(T)$ effect, we adopted this approach for the wide-bandgap CIGSe. A relatively shallow trap energy is necessary in order to allow for re-emission of electrons at high temperature. The temperature dependency of $J_{SC}(T)$ is related to the relative position of the defect level where a deeper defect induces a stronger temperature dependence of $J_{SC}(T)$. Therefore, in our simulation, a defect state 0.2 eV below the conduction band instead of 0.3 eV in a previous study[32] was programmed. Further studies are necessary that may resolve the microscopic origin of this defect.

Over all, it is found that NaF and KF treatments can improve the solar cell parameters of wide-bandgap CIGSe. For all KF-PDT thicknesses, a too high NaF-PDT thickness can deteriorate V_{OC}, probably due to an overly high doping concentration and thus high interface recombination (small type inversion of the absorber surface). However, cells with too little Sodium also exhibit poor performance possibly also due to high interface recombination. It has been surmised that Sodium has an ambiguous role for interface recombination and can also lead to passivation of the front surface[47] and back contact.[48] In effect, there is an optimum NaF-PDT thickness. There is also an optimum KF-PDT thickness balancing between low V_{OC} due to strong interface recombination when the amount of the supplied KF is too low (no conformal SL coverage) and a poor fill factor due to a barrier for the injection current if the supplied KF amount is too large as discussed in Section 4.3. The positive heavy alkali effect is somewhat in contrast to pure $CuGaSe_2$ absorbers where (in the case of RbF) no V_{OC} increase was observed.[49] The reason may be the missing SL formation.[50]

6 | CONCLUSION

Alkalis have different influences on the properties of wide bandgap CIGSe solar cells. Sodium present during the growth reduces the grain size and impedes chemical diffusion. The latter results in a strong Gallium gradient in films grown by the three-stage coevaporation process. The Gallium gradient can be adjusted by coevaporation of Gallium in the second stage, which improves the fill factor of the solar cells. Avoiding Sodium diffusion from the glass requires postdeposition treatment with NaF. Postdeposition with KF further increases the V_{OC} relatively independent on the Cu content in the films. There is an optimum NaF and KF thickness. Too large KF thickness reduces the fill factor, probably due to the formation of a barrier for the injection current at the front contact. This barrier can also explain the double-diode behavior at low temperature as well as the saturation of $V_{OC}(T)$ at low temperature: two specific features that may not necessarily reduce the device efficiency at room temperature. Under standard test conditions, the voltage deficit is the limiting quantity for wide-bandgap CIGSe, with KF to smaller extend than without KF treatment.

ACKNOWLEDGMENT

This work was carried out within the framework of the Federal Ministry for Economic Affairs and Energy (BMWi project EFFCIS under contract 0324076C). Open access funding enabled and organized by Projekt DEAL.

ORCID

Setareh Zahedi-Azad https://orcid.org/0000-0001-7801-6166
Roland Scheer https://orcid.org/0000-0001-5007-3425

REFERENCES

1. Jackson P, Wuerz R, Hariskos D, Lotter E, Witte W, Powalla M. Effects of heavy alkali elements in Cu (In,Ga)Se2 solar cells with efficiencies up to 22.6%. *phys status solidi (RRL) – Rapid Res Lett*. 2016;10 (8):583-586.
2. Chirilă A, Reinhard P, Pianezzi F, et al. Potassium-induced surface modification of Cu(In,Ga)Se2 thin films for high-efficiency solar cells. *Nat Mater*. 2013;12(12):1107-1111.
3. Shockley W, Queisser HJ. Detailed balance limit of efficiency of p-n junction solar cells. *J Appl Phys*. 1961;32(3):510-519.
4. Zahedi-Azad S, Maiberg M, Clausing R, Scheer R. Influence of heavy alkali post deposition treatment on wide gap Cu(In,Ga)Se2. *Thin Solid Films*. 2019;669:629-632.
5. Lundberg O, Edoff M, Stolt L. The effect of Ga-grading in CIGS thin film solar cells. *Thin Solid Films*. 2005;480-481:520-525.
6. Chirilă A, Buecheler S, Pianezzi F, et al. Highly efficient Cu(In,Ga)Se2 solar cells grown on flexible polymer films. *Nat Mater*. 2011;10(11): 857-861.
7. Dullweber T, Anna GH, Rau U, Schock HW. A new approach to high-efficiency solar cells by band gap grading in Cu (In,Ga)Se2 chalcopyrite semiconductors. *Sol Energy Mater Sol Cells*. 2001;67(1-4): 145-150.
8. Gloeckler M, Sites JR. Band-gap grading in Cu(In,Ga)Se2 solar cells. *J Phys Chem Solids*. 2005;66(11):1891-1894.
9. Rudmann D, Bilger G, Kaelin M, Haug F-J, Zogg H, Tiwari AN. Effects of NaF coevaporation on structural properties of Cu(In,Ga)Se2 thin films. *Thin Solid Films*. 2003;431-432:37-40.
10. Ishizuka S, Yamada A, Islam MM, et al. Na-induced variations in the structural, optical, and electrical properties of Cu(In,Ga)Se2 thin films. *J Appl Phys*. 2009;106(3):034908. https://doi.org/10.1063/1.3190528
11. Rudmann D, Bremaud D, Cunha AFD, et al. Sodium incorporation strategies for CIGS growth at different temperatures. *Thin Solid Films*. 2005;480:55-55. https://doi.org/10.1016/j.tsf.2004.11.071
12. Wuerz R, Eicke A, Kessler F, Rogin P, Yazdani-Assl O. Alternative sodium sources for Cu(In,Ga)Se2 thin-film solar cells on flexible substrates. *Thin Solid Films*. 2011;519(21):7268-7271.
13. Zahedi-Azad S, Scheer R. Quenching interface recombination in wide bandgap Cu(In,Ga)Se2 by potassium treatment. *phys status solidi c*. 14 (2017):1600203. https://doi.org/10.1002/pssc.201600203
14. Lepetit T, Harel S, Arzel L, Ouvrard G, Barreau N. KF post deposition treatment in co-evaporated Cu(In,Ga)Se2thin film solar cells: Beneficial or detrimental effect induced by the absorber characteristics. *Prog Photovolt: Res Appl*. 2017;25(12):1068-1076.
15. Weiss TP, Nishiwaki S, Bissig B, et al. Injection current barrier formation for RbF postdeposition-treated Cu(In,Ga)Se2-based solar cells. *Adv Mater Interfaces*. 2018;5(4):1701007. https://doi.org/10.1002/admi.201701007

16. Jackson P, Hariskos D, Wuerz R, et al. Properties of Cu(In,Ga)Se2 solar cells with new record efficiencies up to 21.7%. *phys status solidi (RRL) – Rapid Res Lett*. 2015;9(1):28-31.
17. Orgis T, Maiberg M, Scheer R. Influence of band gradients on CIGS solar cell diode factors. *J Appl Phys*. 2013;114(21):214506. https://doi.org/10.1063/1.4840995
18. Maiberg M. *Numerical and Analytical Study of Time-Resolved Luminescence in Thin-Film Semiconductors, Dissertation*. Martin-Luther-Universität Halle-Wittenberg; 2016.
19. Bodegard M, Granath K, Stolt L. Growth of Cu(In,Ga)Se 2 thin films by coevaporation using alkaline precursors. *Thin Solid Films*. 2000;361-362:9-16.
20. Rudmann D, Cunha AFD, Kaelin M, et al. Efficiency enhancement of Cu (In,Ga)Se_2 solar cells due to post-deposition Na incorporation. *Appl Phys Lett*. 2004;84(7):1129-1131.
21. Zahedi-Azad S, Maiberg M, Clausing R, Scheer R. Influence of heavy alkali post deposition treatment on wide gap Cu (In,Ga)Se_2. *Thin Solid Films*. 2018;669:629-632.
22. Witte W, Abou-Ras D, Albe K, et al. Gallium gradients in Cu(In,Ga) Se2thin-film solar cells. *Prog Photovolt: Res Appl*. 2015;23(6):717-733.
23. Niemegeers A, Burgelman M, Herberholz R, Rau U, Hariskos D, Schock H-W. Model for electronic transport in Cu(In,Ga)Se2 solar cells. *Prog Photovolt: Res Appl*. 1998;6(6):407-421.
24. Eisgruber IL, Granata JE, Sites JR, Hou J, Kessler J. Blue-photon modification of nonstandard diode barrier in $CuInSe_2$ solar cells. *Sol Energy Mater Sol Cells*. 1998;53(3-4):367-377.
25. Gloeckler M, Jenkins CR, Sites JR. Explanation of light/dark superposition failure in CIGS solar cells. *Mater Res Soc Symp Proc*. 2003;763: pp. B5.20.21. https://doi.org/10.1557/PROC-763-B5.20
26. Pianezzi F, Reinhard P, Chirilă A, et al. Unveiling the effects of post-deposition treatment with different alkaline elements on the electronic properties of CIGS thin film solar cells. *Phys Chem Chem Phys*. 2014;16(19):8843-8851.
27. Kodalle T, Bertram T, Schlatmann R, Kaufmann CA. Effectiveness of an RbF post deposition treatment of CIGS solar cells in dependence on the Cu content of the absorber layer. *IEEE J Photovolt*. 2019;9(6):1839-1845.
28. Scheer R, Schock H-W. *Chalcogenide Photovoltaics-Physics, Technologies, and Thin Film Devices*. Wiley VCH: Weinheim; 2011.
29. Wilhelm H, Schock H-W, Scheer R. Interface recombination in heterojunction solar cells: influence of buffer layer thickness. *J Appl Phys*. 2011;109(8):084514. https://doi.org/10.1063/1.3554409
30. Pudov AO, Sites JR, Contreras MA, Nakada T, Schock HW. CIGS J–V distortion in the absence of blue photons. *Thin Solid Films*. 2005;480-481:273-278.
31. Igalson M, Bodegard M, Stolt L. Reversible changes of the fill factor in the ZnO/CdS/Cu(In,Ga)Se2 solar cells. *Sol Energy Mater Sol Cells*. 2003;80(2):195-207.
32. Pianezzi F, Reinhard P, Chirilă A, et al. Defect formation in Cu(In,Ga) Se2thin films due to the presence of potassium during growth by low temperature co-evaporation process. *J Appl Phys*. 2013;114(19):194508. https://doi.org/10.1063/1.4832781
33. Kanevce A, Gloeckler M, Pudov AO, Sites JR. Conduction-band-offset rule governing J-V distortion in CdS/CI(G)S solar cells. *MRS Proc*. 2005;865:F5.32.
34. Siebentritt S. Wide gap chalcopyrites: material properties and solar cells. *Thin Solid Films*. 2002;403-404:1-8.
35. Gloeckler M, Sites JR. Efficiency limitations for wide-band-gap chalcopyrite solar cells. *Thin Solid Films*. 2005;480-481:241-245.
36. Handick E, Reinhard P, Alsmeier J-H, et al. Potassium postdeposition treatment-induced band gap widening at Cu(In,Ga)Se2 surfaces–reason for performance leap? *ACS Appl Mater Interfaces*. 2015;7(49):27414-27420.
37. Hauschild D, Kreikemeyer-Lorenzo D, Jackson P, et al. Impact of a RbF postdeposition treatment on the electronic structure of the CdS/Cu(In,Ga)Se2 heterojunction in high-efficiency thin-film solar cells. *ACS Energy Lett*. 2017;2(10):2383-2387.
38. Ott T, Schönberger F, Walter T, et al. Verification of phototransistor model for Cu(In,Ga)Se 2 solar cells. *Thin Solid Films*. 2015;582:392-396.
39. Ott T, Walter T, Unold T. Phototransistor effects in Cu(In,Ga)Se2 solar cells. *Thin Solid Films*. 2013;535:275-278.
40. Avancini E, Carron R, Weiss TP, et al. Effects of rubidium fluoride and potassium fluoride postdeposition treatments on Cu(In,Ga)Se2 thin films and solar cell performance. *Chem Mater*. 2017;29(22):9695-9704.
41. Handick E, Reinhard P, Alsmeier J-H, et al. Potassium postdeposition treatment-induced band gap widening at Cu(In,Ga)Se_2 surfaces–reason for performance leap? *ACS Appl Mater Interfaces*. 2015;7(49):27414-27420.
42. Kodalle T, Kormath Madam Raghupathy R, Bertram T, et al. Properties of co-evaporated RbInSe2 thin films. *phys status solidi (RRL) – Rapid Res Lett*. 2019;13:1800564. https://doi.org/10.1002/pssr.201800564
43. Nicoara N, Lepetit T, Arzel L, Harel S, Barreau N, Sadewasser S. Effect of the KF post-deposition treatment on grain boundary properties in Cu(In,Ga)Se2 thin films. *Sci Rep*. 2017;7(1):41361. https://doi.org/10.1038/srep41361
44. Pistor P, Greiner D, Kaufmann CA, et al. Experimental indication for band gap widening of chalcopyrite solar cell absorbers after potassium fluoride treatment. *Appl Phys Lett*. 2014;105(6):063901. https://doi.org/10.1063/1.4892882
45. Ishizuka S, Taguchi N, Fons PJ. Similarities and critical differences in heavy alkali-metal rubidium and cesium effects on chalcopyrite Cu(In,Ga)Se2 thin-film solar cells. *J Phys Chem C*. 2019;123(29):17757-17764.
46. Cojocaru-Mirédin O, Choi P, Abou-Ras D, Schmidt SS, Caballero R, Raabe D. Characterization of grain boundaries in Cu(In,Ga)Se2 films using atom-probe tomography. *IEEE J Photovoltaics*. 2011;1(2):207-212.
47. Hölscher T, Schneider T, Maiberg M, Scheer R. Impact of air-light exposure on the electrical properties of Cu(In,Ga)Se2solar cells. *Prog Photovolt: Res Appl*. 2018;26(11):934-941.
48. Jarzembowski E, Syrowatka F, Kaufmann K, Fränzel W, Hölscher T, Scheer R. The influence of sodium on the molybdenum/Cu(In,Ga)Se2 interface recombination velocity, determined by time resolved photoluminescence. *Appl Phys Lett*. 2015;107(5):051601. https://doi.org/10.1063/1.4928187
49. Ishizuka S, Taguchi N, Nishinaga J, Kamikawa Y, Tanaka S, Shibata H. Group III elemental composition dependence of RbF postdeposition treatment effects on Cu(In,Ga)Se2 Thin films and solar cells. *J Phys Chem C*. 2018;122(7):3809-3817.
50. Taguchi N, Tanaka S, Ishizuka S. Direct insights into RbInSe2 formation at Cu(In,Ga)Se2 thin film surface with RbF postdeposition treatment. *Appl Phys Lett*. 2018;113(11):113903.

SUPPORTING INFORMATION

Additional supporting information may be found online in the Supporting Information section at the end of this article.

How to cite this article: Zahedi-Azad S, Maiberg M, Scheer R. Effect of Na-PDT and KF-PDT on the photovoltaic performance of wide bandgap Cu (In,Ga)Se2 solar cells. *Prog Photovolt Res Appl*. 2020;28:1146–1157. https://doi.org/10.1002/pip.3317